Non-invasive in situ concentration determination of fluorescent or color tracers and pollutants in a glass pore network model

3 AUTHORS, INCLUDING:

Constantinos V. Chrysikopoulos
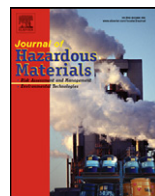Technical University of Crete
143 PUBLICATIONS **1,994** CITATIONS

Vasileios Katzourakis
University of Patras
8 PUBLICATIONS **17** CITATIONS

Non-invasive in situ concentration determination of fluorescent or color tracers and pollutants in a glass pore network model

Constantinos V. Chrysikopoulos *, Christina C. Plega, Vasileios E. Katzourakis

Department of Civil Engineering, Environmental Engineering Laboratory, University of Patras, Patras 26500, Greece

ABSTRACT

This study presents a non-invasive imaging method for in situ concentration determination of conservative tracers and pollutants in a two-dimensional glass pore network model. The method presented is an extension to the work by Huang et al. [1], and Thomas and Chysikopoulos [2]. The method consists of fabricating the glass pore network model using a photolithography technique, conducting flowthrough contaminant transport experiments, taking digital photographs at various times of the two-dimensional pore network under ultraviolet or visible light source, and determining the spatially-distributed pollutant concentrations by measuring the color intensity in the photographs with comparative image analysis. Therefore, the method is limited to fluorescent or colored pollutants and tracers. The method was successfully employed to in situ concentration determination of uranine and red color tracers.

© 2011 Elsevier B.V. All rights reserved.

1. Introduction

Several non-invasive imaging methods have been developed in the recent years for a variety of solute transport and porous media characterization. The majority of these methods employ optical, magnetic resonance, and gamma radiation techniques. An excellent comparison of the various non-invasive imaging methods available for subsurface contaminant migration applications was presented in the review paper by Werth et al. [3]. For direct and clear viewing of solute and particle movement, as well as two-phase immiscible flow within a complex pore space, micromodels are often employed instead of packed columns. Micromodels are transparent networks of pores and constrictions that simulate some of the complexities of natural porous media. Numerous visualization flow and transport in porous media studies presented in the literature employ etched micromodels [4–12] or monolayers of glass beads [13–15].

An imaging procedure using ultraviolet (UV) illumination has been reported by Huang et al. [1] in order to evaluate the transport of fluorescein in a transparent plastic (Perspex) box with internal dimensions $18 \times 28 \times 1$ cm, packed with glass beads. The procedure consisted of illuminating the fluorescein with UV light, capturing the emitted fluorescence by a camera, and converting image intensities to fluorescein concentrations. The procedure was shown to

be simple and moderately accurate, but limited to fluorescent tracers. Recently, Thomas and Chrysikopoulos [2] developed a method for accurate in situ measurement of conservative tracer and colloid concentrations in columns packed with glass beads. The method consists of fabricating clear sintered glass-bead-packed columns, by taking digital photographs of the column under a UV light source, and determining concentrations by measurement of the fluorescence intensity of the tracer or colloids in the photographs. The method was shown to be as accurate as standard effluent sampling and is capable of capturing concentration data at multiple time steps, but it is limited to one-dimensional packed columns. The objective of this research is to extend the work by Huang et al. [1], and Thomas and Chrysikopoulos [2] to the case of in situ measurement of conservative red color (rc) tracer and uranine (u) concentrations in two-dimensional etched micromodels under ultraviolet or visible light sources and to eliminate errors that could occur in previous studies due to image blurring caused by optical dispersion through glass-bead-packed porous medium, and solute distribution within the thickness of the porous medium.

2. Procedures and materials

2.1. Micromodel fabrication

The selected micromodel pore network was carefully designed with AutoCAD® and was printed on a high quality transparent sheet of acrylic film. The transparent pore network pattern, shown in

---

* Corresponding author. Tel.: +30 2610 996531; fax: +30 2610 996573.
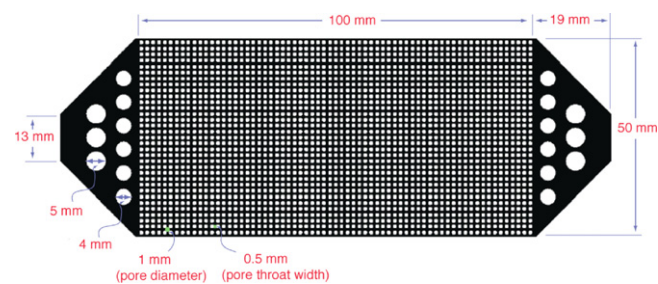E-mail address: gios@upatras.gr (C.V. Chrysikopoulos).

Fig. 1. Computer image ("mask") of the pore network micromodel. The dark areas correspond to the voids of the micromodel. There are 67 pore bodies along the x-direction is 67 and 34 along the y-direction.

Fig. 1, was used as a photographic "mask". Therefore, the dark areas in the mask represent the void spaces of the micromodel. The dimensions of the pore network are $L_x = 100$ mm in length and $L_y = 50$ mm in width. The diameter of each pore (pore body) is 1 mm, and the width of the narrow channels (or pore throats) connecting the pores in a square lattice arrangement is 0.5 mm. The larger voids at the two ends of the micromodel were included in order to aid in the uniform distribution of the incoming fluids.

The micromodel was constructed with the photolithographic technique developed by McKellar and Wardlaw [16] with certain modifications initially proposed by Payatakes and co-workers [17–19]. The method consists of a photo-imaging procedure followed by chemical etching of the glass. Two pieces of mirror glass with approximate dimensions 21 cm in length and 12 cm in width were placed in 600 mL single-distilled water (sdH$_2$O) solution containing 200 g NaOH for a 24 h time period, in order to remove the protective layer of the mirror and to expose the copper. Then, the mirrors were gently washed with sdH$_2$O, and were placed in a dark and dust-free room where the copper surfaces were sprayed with Positive Resist (Cramolin, Germany) until a visible film had built up. Subsequently, the mirrors were placed for 30 min in a furnace, which was preheated at 70 °C, in order to allow the film to dry. The Positive Resist was used because it offers a convenient way to accurately copy any illustration onto a great variety of materials and ensures relatively fast drying and high sharpness. Each glass essay was allowed to cool off, and the network "mask" was adapted on the surface with the Positive Resist film. The glass essays were exposed for 45 min to ultraviolet light in a custom-made large wooden container were the visible Positive Resist film was polymerized. Subsequently, the glass essays were retained in dark room, and they were placed in a sdH$_2$O bath containing 7 g/L NaOH for a few minutes (<10 min) to dissolve the non-polymerized Positive Resist film. The precise bathing period was determined by visual inspection under the red light (Philips darkroom lamp 230 V). This was the last visible-light sensitive step. Next, the glass essays were washed with sdH$_2$O and placed in a HNO$_3$ solution bath (200 mL HNO$_3$ 65% and 230 mL sdH$_2$O) for approximately 10 s to dissolve the copper surface area, which is no longer covered by the Positive Resist film. Then, pre-heated wax was carefully spread to form a layer over the glass essay area surrounding the pore network that should not be etched. Additional wax was placed at the four edges of the glass essay in order to form a thick wall capable of retaining approximately 30 mL of fluids at the top surface of the glass essay. Subsequently, 20 mL of HF solution (prepared with 75 mL HF 90% in 25 mL sdH$_2$O) were poured on the waxed surface of the glass essay for 5 min. The glass essays were thoroughly washed with sdH$_2$O and the wax was carefully removed. Subsequently, the glass essays were placed in a HNO$_3$ solution until all of the remaining copper was removed. Then, the transparent glass essays were washed with sdH$_2$O. Prior to sintering, two holes were carefully drilled in one of the two etched glasses
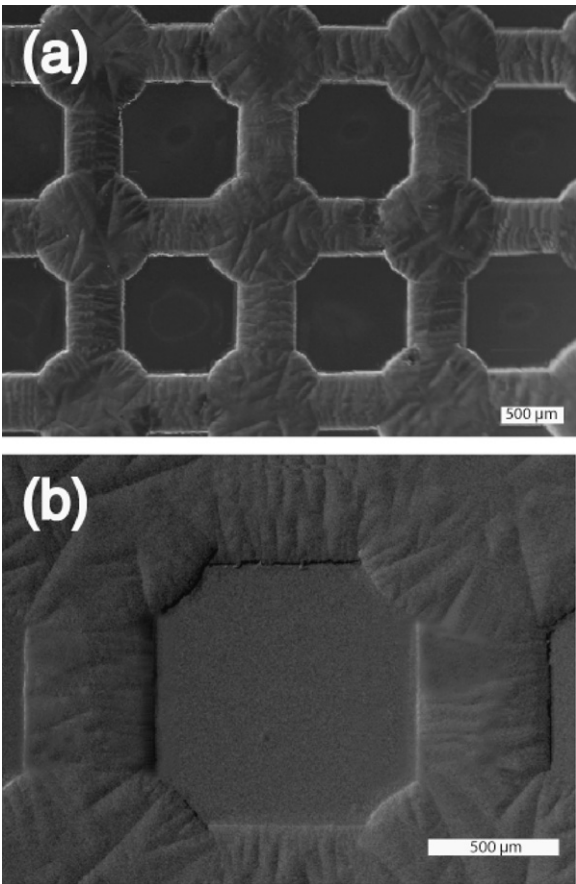

Fig. 2. Scanning electron micrographs of (a) a selected micromodel section, and (b) four connected pores in a square lattice.

in order to create the necessary inlet and outlet openings of the micromodel. Finally, the desired two-dimensional micromodel was constructed by sintering the two etched glasses in a programmable furnace. Based on numerous preliminary sintering tests, the furnace was programmed to the following temporal temperature variation: 2 min at 40 °C, 6 h at 400 °C, 2 h at 500 °C, 2 h at 600 °C, 30 min at 690 °C, and 30 min at 600 °C. Scanning electron microscope (SEM) images of the etched micromodel are presented in Fig. 2. However, it should be noted that one significant limitation of the method presented is that pores with radius <20 μm are quite difficult to be etched with great precision on the glass essay.

The porosity, pore volume, pore depth, and cross sectional area of the micromodel, listed in Table 1, were determined by both simple geometric considerations and by direct use of the line scan option of SEM. However, it should be noted that the pore depth value listed in Table 1 is a spatially averaged value, because the micromodel fabrication technique employed does not guarantee a spatially uniform pore depth. The intrinsic permeability, k [L^2], of the micromodel was determined by conducting flow through

Table 1
Parameters of the pore network micromodel.

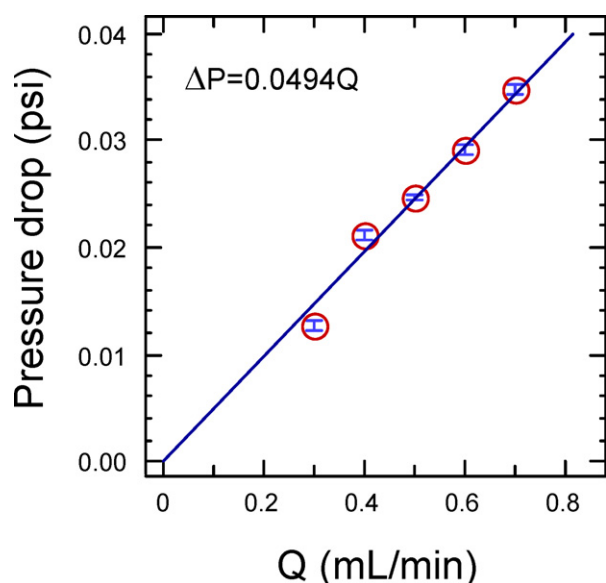| Parameter	Symbol	Value
Length	L_x	10 cm
Width	L_y	5 cm
Porosity	θ	59.2%
Pore depth	L_p	390.2 μm
Pore volume	V_p	1.184 cm^3
Cross sectional area	A_m	1.95×10^{-5} m^2
Intrinsic permeability	k	2.23×10^{-10} m^2

Fig. 3. Pressure drop variation with increasing volumetric flow rate. The error bars are also shown and they are smaller than the symbols.

Fig. 4. Schematic illustration of the experimental setup.

experiments with sdH$_2$O at various volumetric flow rates, Q [L^3/t], and measuring the pressure drop, ΔP [M/(t^2 L)], across the length of the micromodel with pressure sensors. The experimental results for five different Q values are shown in Fig. 3. The k value of the micromodel was determined from Darcy's law [20]:

$$Q = -A_m \left(\frac{k\gamma_w}{\mu_w} \right) \frac{\Delta h}{\Delta x} \Rightarrow k = -\mu_w \frac{\Delta x}{A_m} \left(\frac{Q}{\Delta P} \right) \quad (1)$$

where $A_m = L_y \times L_p$ [L^2] is the cross sectional area of the micromodel (L_p [L] is the pore depth of the micromodel), γ_w [M/(t^2 L^2)] is the specific weight of the interstitial fluid, μ_w [M/(t L)] is the dynamic viscosity of the interstitial fluid, $\Delta h = \Delta P/\gamma_w$ [L] is the head drop along the length of the micromodel, and $\Delta x = L_x$ [L] is the length of the micromodel. Given that the slope of the fitted line in Fig. 3 was estimated to be $\Delta P/Q = 0.0494$ psi/(mL/min), the dynamic viscosity of water at 25 °C is $\mu_w = 0.89 \times 10^{-3}$ (N s)/m^2 [21], and 1 psi = 6894.7 N/m^2, the intrinsic permeability of the micromodel was determined from Eq. (1) as $k = 2.23 \times 10^{-10}$ m^2.

2.2. Experimental setup

The micromodel was placed on top of a light table equipped with two sets of light sources using (a) visible light (Philips TLD graphica Pro 18 W/95), and (b) ultraviolet (UV) light (Philips Black Light lamps). Fluids were inserted in the micromodel with a syringe pump (Cole-Parmer 74900) placed at the exact same vertical level with the micromodel. Tracer solutions were injected into the micromodel through an injection port mounted at the micromodel inlet with a plastic 1 mL syringe. A digital camera (Nikon D5000) mounted on a tripod was placed directly above the micromodel. Any digital camera will work as long as it has a color mode that employs the red-green-blue (RGB) color space, and the ability to both automatically and manually set aperture, shutter speed, camera sensitivity based on International Standards Organization (ISO) speed numbers, and focus. The ability of the camera to take a series of photographs on a set time interval is convenient, but not essential [2]. A schematic illustration of the experimental apparatus is shown in Fig. 4. To avoid any undesired ambient light, the experimental apparatus were situated in a convenient dark room.

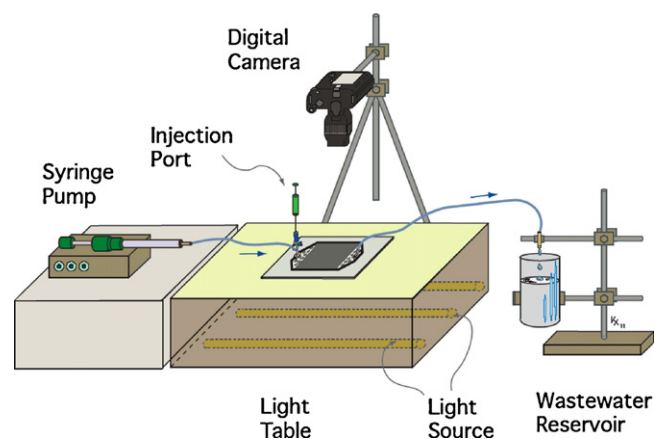Prior to conducting each experiment, the micromodel was fully saturated with sdH$_2$O. At least 10 pore volumes of sdH$_2$O were flushed through the micromodel to remove any air bubbles. After steady state flow conditions were established, the solution of the desired solute was injected into the water-saturated micromodel.

2.3. Setting the digital camera

A few preliminary steps were completed before the initiation of each experiment to ensure that all photographs could be directly compared to one another without any scaling adjustments and that the maximum recordable intensity value of the digital camera was never exceeded. First, the digital camera was set to the auto exposure and natural color mode (RGB color space), and a photograph of the solution injected into the micromodel was taken. The concentration of the solute was exactly the same as that to be used in the experiment. The intensity of light emitted from the solute was recorded for each pixel. Note that in this first photograph, the injected solution was most concentrated and the observed intensity was at the maximum expected level. Therefore, this photograph allowed to the digital camera to determine the proper aperture, shutter speed, and necessary ISO sensitivity, so that the maximum recordable intensity value would not be exceeded, because all subsequent photographs were expected to have equal or lower recorded intensity for each pixel due to solute dilution caused by hydrodynamic dispersion within the micromodel. Then, these settings were recorded and used to set the digital camera at its manual mode. Finally, the digital camera was also manually focused, in order to maintain the exact same focus throughout the experiment.

2.4. Background image

Prior to running an experiment the micromodel was cleaned by flushing at least 10 pore volumes of sdH$_2$O. Subsequently, a photograph was taken of the water-saturated micromodel in the absence of any solute with the previously determined camera settings and the desired light source (visible or UV). This picture constituted the "background image" and was used in the subsequent analysis of photographic images taken after the injection of the solute into the micromodel.

2.5. Image processing

The photographic images taken of the tracer solutions within the micromodel were processed using the MATLAB® Image Processing Toolbox™ following the procedures employed by Bouhairie [22], and Thomas and Chrysikopoulos [2]. The basic data structure in MATLAB® is the array, which is an ordered set of real or complex elements. Similarly, an RGB image is essentially stored as a

three-dimensional array consisting of three two-dimensional (2-D) arrays of pixel intensities, one for red, one for green, and one for blue. Each 2-D array has x and y dimensions corresponding to the rows and columns of pixels in the image with an intensity value on a scale from 0 to 255 stored in each location. These images can be manipulated with matrix operations, and light intensities can be converted to concentrations. The total number of pixels, and compression rate (image quality) of the image were set in the camera. Note that the actual area covered by the pixels was altered as the digital camera was zoomed in or out. For this reason it was essential to map the pixels in the images to actual locations within the 2-D surface area of the micromodel, by assigning appropriate coordinates to each pixel (i.e., x-direction, and y-direction). This was accomplished by using the 'imtool' function of the MATLAB® Image Processing Toolbox™ to count the number of pixels along the length and width of the micromodel. The actual micromodel length per pixel was obtained by dividing the micromodel length (100 mm) by the number of pixels in the x-direction, and the actual micromodel width per pixel was obtained by dividing the micromodel width (50 mm) by the number of pixels in the y-direction. Next, the background images taken at the beginning of the experiments were subtracted from each of the subsequent images using the 'imsubtract' function MATLAB® Image Processing Toolbox™. The resultant images consisted only of the visible or fluorescent light emitted from the tracers examined.

2.6. Calibration curve

To correlate the pixel intensities (scaled from 0 to 255) of the photographic images to actual tracer concentrations in the micromodel, a calibration curve was required for each solute utilized. The necessary calibration curves were constructed with a straightforward procedure. A standard solution was prepared and diluted to several different but known solute concentrations. Using the previously determined digital camera settings, a photographic image was captured of the micromodel, which was fully saturated with the lowest standard solute concentration. Then, the micromodel was saturated with the next standard tracer concentration and another photographic image was captured. The procedure was repeated until all of the known solute concentrations were used. The desired calibration curve was constructed by plotting the known solute concentrations against the recorded image intensities. The calibration curve was used to quantify all pixel intensities from photographic images recorded in subsequent experiments utilizing the same solute.

3. Mathematical model

Two-dimensional solute transport in homogeneous, water saturated porous media is governed by the following partial differential equation:

$$\frac{\partial C(t,x,y)}{\partial t} = D_L \frac{\partial^2 C(t,x,y)}{\partial x^2} + D_T \frac{\partial^2 C(t,x,y)}{\partial y^2} - U \frac{\partial C(t,x,y)}{\partial x} \quad (2)$$

where C [M/L³] is the solute concentration; D_L [L²/t] and D_T [L²/t] are the longitudinal and transverse hydrodynamic dispersion coefficients [17]:

$$D_L = \alpha_L U + D_e \quad (3)$$

$$D_T = \alpha_T U + D_e \quad (4)$$

where α_L [L/t] is the longitudinal dispersivity; α_T [L/t] is the transverse dispersivity; $D_e = D_{AB}/\tau^*$ [L²/t] is the effective molecular diffusion coefficient ($\tau^* \geq 1$ [–] is the tortuosity coefficient, and D_{AB} [L²/t] is the molecular diffusion coefficient); U [L/t] is the interstitial velocity; x [L] and y [L] are the Cartesian coordinates; and t
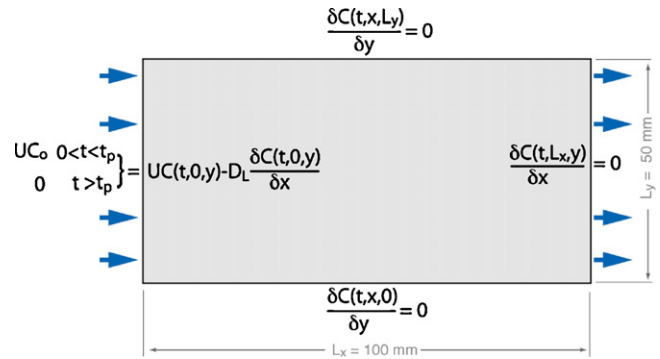

Fig. 5. Transport domain and boundary conditions used for the numerical solution.

[t] is time. The micromodel interstitial velocity can be calculated using the expression

$$U = \frac{Q}{A_m \theta} \quad (5)$$

where θ [–] is the porosity of the micromodel. The molecular diffusion coefficient of a solute can be estimated using the Wilke–Chang relationship [23]:

$$D_{AB} = 7.4 \times 10^{-8} \frac{(\psi_B m w_B)^{1/2} T}{\mu_B V_A^{0.6}} \quad (6)$$

where A is the solute; B is the solvent (water); $\psi_B = \psi_{H_2O} = 2.6$ is an association parameter for solvent B [24]; $\mu_B = \mu_w = 0.890 \times 10^{-3}$ (N s)/m² = 0.89 cp is the water viscosity at 25 °C in units of centipoises (1 cp = 0.001 (N s)/m²), $m w_B = 18$ g/mol is the molecular weight of water, T [K] is the absolute temperature, and $V_A = m w_A/\rho_A$ [cm³/g mol] is the molar volume of solute A.

The initial condition for the physical problem examined in this study is

$$C(0,x,y) = 0 \quad (7)$$

and the appropriate boundary conditions are

$$-D_L \frac{\partial C(t,0,y)}{\partial x} + UC(t,0,y) = \begin{cases} UC_0 & 0 < t \leq t_p \\ 0 & t > t_p \end{cases} \quad (8)$$

$$\frac{\partial C(t,x,0)}{\partial y} = \frac{\partial C(t,x,L_y)}{\partial y} = 0 \quad (9)$$

$$\frac{\partial C(t,L_x,y)}{\partial x} = 0 \quad (10)$$

where t_p [t] is the pulse time period. Condition (7) establishes that there is no initial solute concentration within the two-dimensional porous medium. The third- or flux-type boundary condition (8) implies a solute concentration discontinuity at the inlet [25]. Condition (9) implies that there is no solute flux across the lateral boundaries of the two-dimensional porous medium. The downstream boundary condition (10) preserves concentration continuity for a semi-infinite system. Although analytical solutions to solute transport in semi-infinite porous media [9] and bounded domains with point source [26,27] have been presented in the literature, to our knowledge the analytical solution of the partial differential Eq. (2) subject to initial condition (7) and boundary conditions (8)–(10) is not available. Consequently, this problem was solved numerically by the fully implicit finite difference method. The numerical domain is schematically illustrated in Fig. 5.

The tortuosity is a fundamental property of a porous medium, which was introduced by Carman [28] to describe the sinuousness interconnectedness of the pore space. Worthy to note is that the diffusion of a solute in a water saturated porous medium is less rapid

than in pure water because of the restricted free void area available and increased path length. Several tortuosity models based on molecular diffusivity and electrical resistivity are available in the literature [29]. In this study, the tortuosity model introduced by Bruggeman [30] is employed:

$$\tau^* = \theta^{1-\alpha} \approx \frac{1}{\sqrt{\theta}} \tag{11}$$

where α [–] is the Bruggeman exponent, which frequently is employed with the value of $\alpha \approx 1.5$ [31].

4. Application of the method

The non-invasive in situ concentration determination technique described here was used to analyze the migration and spreading of red color and uranine tracers in the micromodel. The red color tracer employed in this study is known as azorubine or carmoisine or Food, Drug and Cosmetic (FD&C) food dye number 3 with color index number 14720 [32] and E122, is a red to maroon powder compound, with molecular formula $C_{20}H_{12}N_2Na_2O_7S_2$, molecular weight 502.44 g/mol, density $\sim$0.45 g/cm^3, and is used for the purposes where the food is heat-treated after fermentation [33]; thus, it is frequently used for traditional Easter egg dyeing. Whereas, uranine, also known as the disodium salt form of fluorescein or FD&C Yellow number 8, with color index number 45350 [32], is an orange-red powdered compound, with molecular formula $C_{20}H_{10}O_5Na_2$, molecular weight 376.28 g/mol, density 1.53 g/cm^3, exhibits intense greenish-yellow fluorescence in alkaline solution, and is frequently used in numerous industrial applications including geothermal and ground water tracing [34]. In view of Eq. (6), the molecular diffusion of red color is estimated to be $D_{AB(rc)} = 2.52 \times 10^{-10}$ m^2/s, and for uranine is $D_{AB(u)} = 6.24 \times 10^{-10}$ m^2/s. Also, in view of Eq. (11), the tortuosity is estimated to be $\tau^* = 1.3$. Therefore, the effective molecular diffusion for the red color is $D_{e(rc)} = 1.94 \times 10^{-10}$ m^2/s, and for uranine is $D_{e(u)} = 4.80 \times 10^{-10}$ m^2/s.

Prior to running experiments with the red color and uranine tracers, the two necessary calibration curves were constructed, and they are presented in Fig. 6. The experiments were conducted following the previously described protocol with a flow rate of $Q = 2$ mL/h. After steady state flow conditions within the micromodel were established, 0.1 mL of the tracer solution was injected into the water-saturated micromodel, over an injection pulse period of $t_p = 12$ min. The concentration of the red color tracer injected into the micromodel was $C_{0(rc)} = 10$ g/L, and the concentration of uranine was $C_{0(u)} = 0.3$ g/L. For each experiment the digital camera was set to capture snapshots at a pre-selected time interval. Each RGB image was separated into red, green, and blue component images. Using the calibration curves (Fig. 6), the color intensities, $I_{(rc)}$ [–], were converted to actual in situ red color concentrations, $C_{(rc)}$ in units of [g/L], using the relationship:

$$C_{(rc)} = -0.19 I_{(rc)} + 28.32 \tag{12}$$

Similarly, the fluorescent intensities, $I_{(u)}$ [–], were converted to actual in situ uranine concentrations, $C_{(u)}$ in units of [g/L], using the relationship:

$$C_{(u)} = 9.3 \times 10^{-4} I_{(u)} - 1.6 \times 10^{-2} \tag{13}$$

Note that the intensity was assumed to be a non-dimensional number as recorded by the camera. Selected photographic images (snapshots) and the corresponding concentration contours for an experiment using the red color tracer with visible light source are presented in Fig. 7, and for uranine with UV source are shown in Fig. 8. Visual inspection of the photographic images and the corresponding concentration contours suggest that the non-invasive concentration determination technique employed in this study is
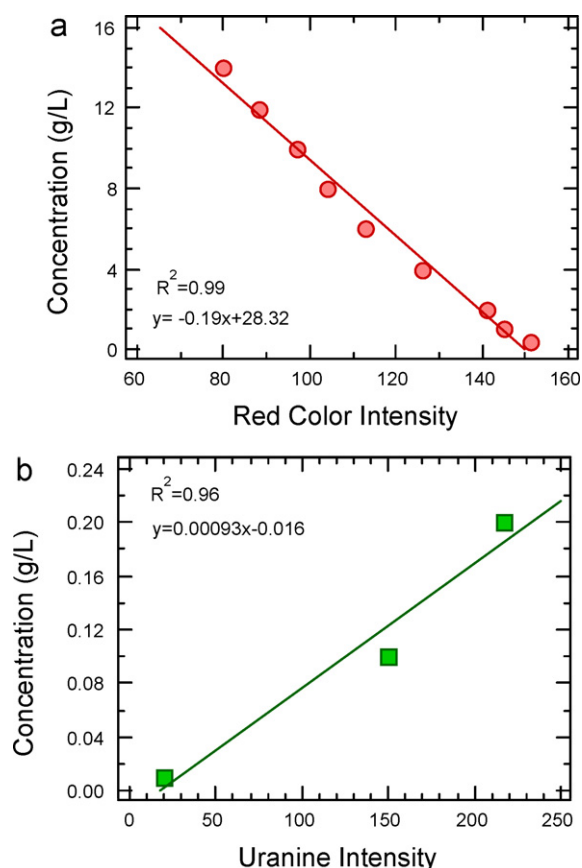

Fig. 6. Concentration calibration curves of the experiments conducted with (a) visible light source, and (b) ultraviolet light source.

more than moderately satisfactory for both color and fluorescent tracers.

To further illustrate the importance of the in situ concentration determination technique presented in this work, the micromodel longitudinal dispersivity was calculated using the experimental data from both of the solute experiments. Accurate prediction of contaminant transport in porous media relies heavily on usage of suitable dispersion coefficients, which are traditionally determined from nonreactive tracer experiments. Numerous laboratory and field scale studies have focused on estimation of either the longitudinal dispersion coefficient [35–41], or the transverse dispersion coefficient [9,42–45]. Hydrodynamic dispersion coefficients are driven by the interplay of fluid motion and molecular diffusion in the pore scale. Worthy to note is that for the estimation of the hydrodynamic dispersion coefficients for solute and contaminant transport in porous media without the use of correlations, which are typically derived from experimental observations, several theoretical and numerical procedures are available in the literature. For periodic media, dispersion coefficient estimation may be determined with volume averaging and generalized Taylor–Aris–Brenner techniques, by defining a representative elementary volume (REV) [46–48]. For non-periodic or heterogeneous porous media, where REV selection may not be a trivial task, random-walk particle tracking methods are often employed [49].

In this study, the intensities obtained at a few randomly selected points within the micromodel were converted to concentrations. The previously described solute transport model was used to fit the experimental concentrations in order to determine the desired transport parameters. For the fitting process the model-independent parameter estimation software PEST was employed. PEST employs the Gauss–Marquardt–Levenberg
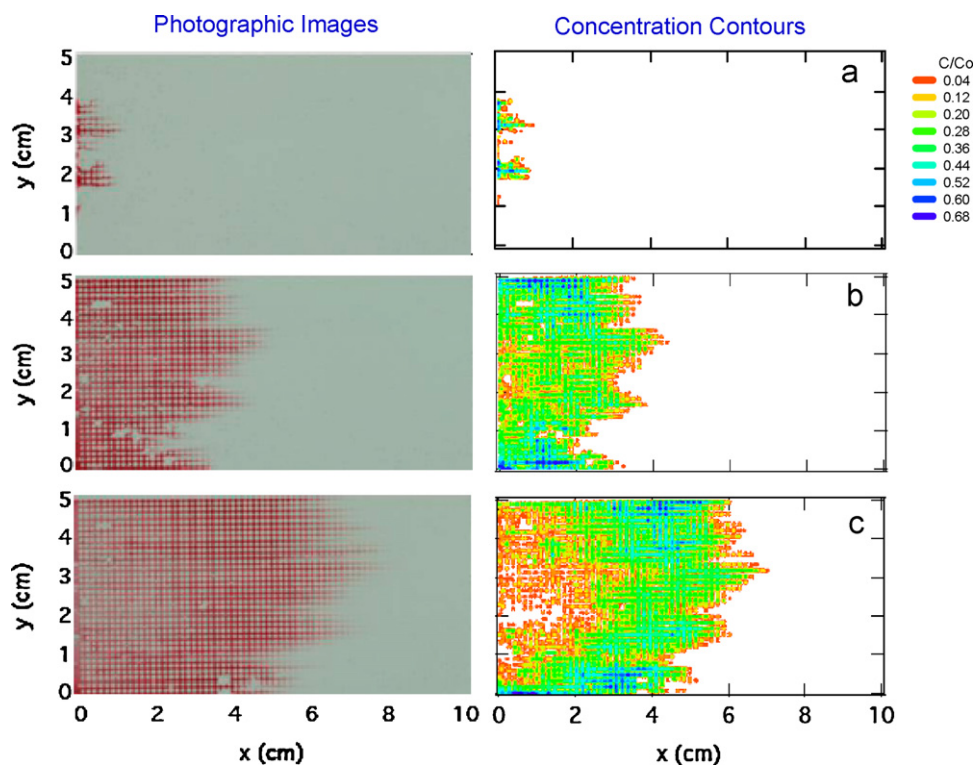
Fig. 7. Photographic images (left column) and concentration contours (right column) of red color tracer injection in the micromodel over a visible light source at (a) 1 min, (b) 4 min, and (c) 7 min.

nonlinear least squares algorithm. The experimental data together with the fitted model simulations are shown in Fig. 9. Clearly, there is very good agreement between the experimental data and the model simulations. The fitted longitudinal dispersion coefficient

for the red color was $D_{L(rc)} = 0.08 \pm 0.03$ cm^2/min, and for uranine is $D_{L(u)} = 0.07 \pm 0.03$ cm^2/min. Note that the transverse dispersion coefficient for both cases examined here was fixed to a zero value ($D_{T(rc)} = D_{T(u)} = 0$). In view of Eqs. (3) and (5), the
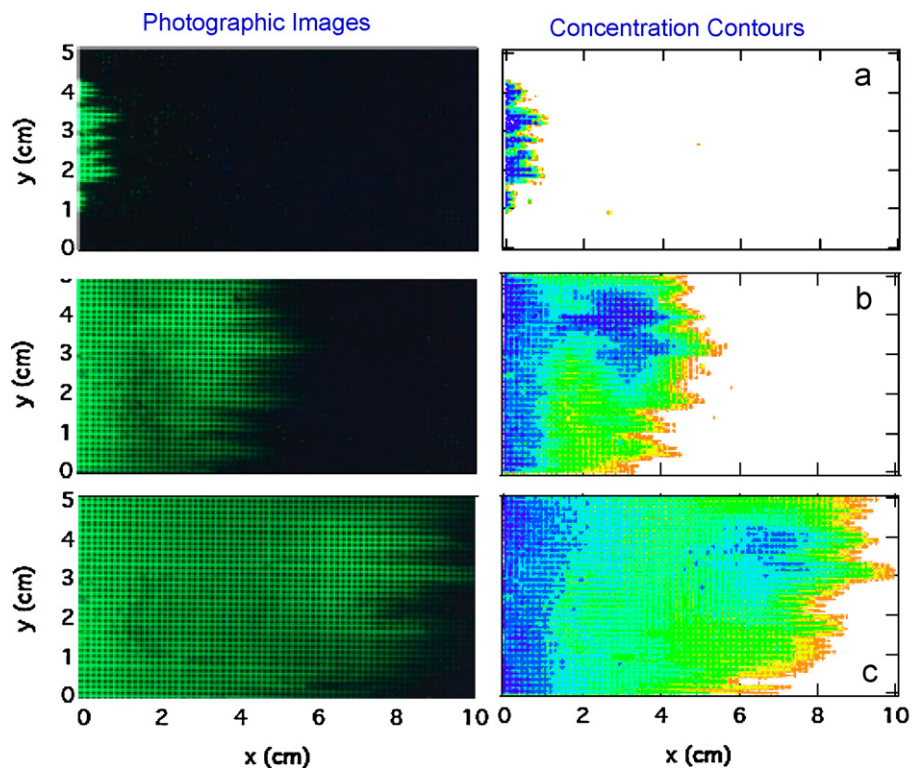

Fig. 8. Photographic images (left column) and concentration contours (right column) of uranine injection in the micromodel over a UV light source at: (a) 1 min, (b) 5 min, and (c) 9 min.
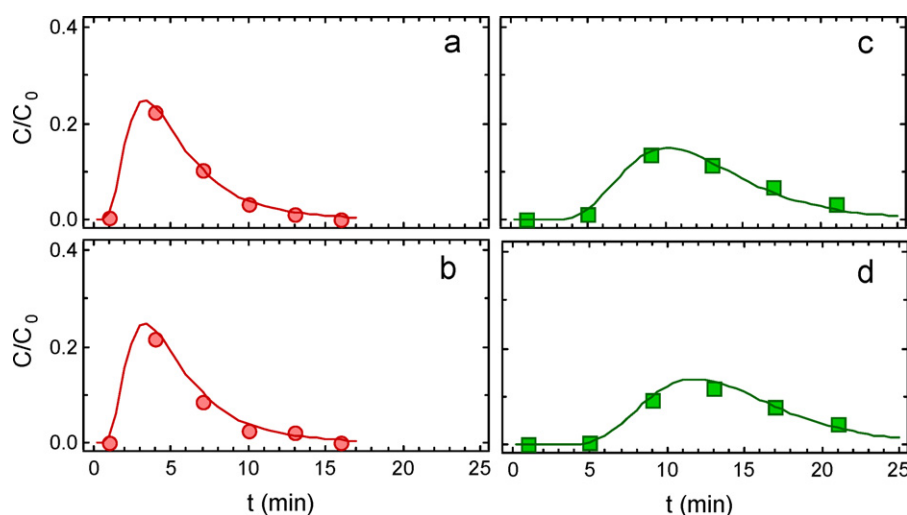
Fig. 9. Concentrations measured in situ for (a and b) red color tracer (circular symbols), and (c and d) uranine (square symbols). The Cartesian coordinates (x, y) of each point of measurement within the micromodel are: (a) (15 mm, 20 mm), (b) (15 mm, 38 mm), (c) (35 mm, 45 mm), and (d) (40 mm, 10 mm). Here $Q = 2$ mL/min or equivalently $U = 0.288$ cm/min, and $t_p = 0.3$ min.

corresponding longitudinal dispersivity using the red color data was estimated to be $\alpha_{L(rc)} = 0.27 \pm 0.09$ cm, and using the uranine data $\alpha_{L(u)} = 0.24 \pm 0.09$ cm. These longitudinal dispersivity values compare well with those reported in the literature for chloride transport in a glass micromodel [50].

5. Summary

The non-invasive imaging method for in situ concentration determination presented by Huang et al. [1], which was limited to fluorescent tracers, and the work by Thomas and Chysikopoulos [2], which was limited to one-dimensional packed columns, was extended. The revised method consisted of conducting flow through experiments in two-dimensional glass pore network models, taking digital photographs, and converting color or UV intensities to concentrations. Consequently, no errors occurred due to image blurring caused by optical dispersion through glass-bead-packed porous medium, and solute distribution within the thickness of the porous medium. The method was shown to be applicable to both color and fluorescent solutes.

References

[1] W.E. Huang, C.C. Smith, D.N. Lerner, S.F. Thornton, A. Oram, Physical modeling of solute transport in porous media: evaluation of an imaging technique using UV excited fluorescent dye, Water Res. 36 (2002) 1843–1853.
[2] J.M. Thomas, C.V. Chrysikopoulos, A new method for *in situ* concentration measurements in packed-column transport experiments, Chem. Eng. Sci. 65 (2010) 4285–4292.
[3] C.J. Werth, C. Zhang, M.L. Brusseau, M. Oostrom, T. Baumann, A review of non-invasive imaging methods and applications in contaminant hydrogeology research, J. Contam. Hydrol. 113 (2010) 1–24.
[4] J. Wan, T.K. Tokunaga, F.C. Tsang, G.S. Bodvarsson, Improved glass micromodel methods for studies of flow and transport in fractured porous media, Water Resour. Res. 32 (1996) 1955–1964.
[5] A.A. Keller, M.J. Blunt, P.V. Roberts, Micromodel observation of the role of oil layers in three-phase flow, Transp. Porous Media 26 (1997) 277–297.
[6] C. Jia, K. Shing, Y.C. Yortsos, Visualization and simulation of non-aqueous phase liquids solubilization in pore networks, J. Contam. Hydrol. 35 (1999) 363–387.
[7] C.D. Tsakiroglou, M. Theodoropoulou, V. Karoutsos, D. Papanicolaou, V. Sygouni, Experimental study of the immiscible displacement of shear-thinning fluids in pore networks, J. Colloid Interface Sci. 267 (2003) 217–232.
[8] S. Sirivithayapakorn, A.A. Keller, Transport of colloids in saturated porous media: a pore-scale observation of the size exclusion effect and colloid acceleration, Water Resour. Res. 39 (2003) 1109, doi:10.1029/2002WR001583.
[9] M.A. Theodoropoulou, V. Karoutsos, C. Kaspiris, C.D. Tsakiroglou, A new visualization technique for the study of solute dispersion in model porous media, J. Hydrol. 274 (2003) 176–197.
[10] T. Baumann, C.J. Werth, Visualization and modeling of polystyrol colloid transport in a silicon micromodel, Vadose Zone J. 3 (2004) 434–443.
[11] M. Auset, A.A. Keller, Pore-scale processes that control dispersion of colloids in saturated porous media, Water Resour. Res. 40 (2004) W03503, doi:10.1029/2003WR002800.
[12] T.M. Willingham, C.J. Werth, A.J. Valocchi, Evaluation of the effects of porous media structure on mixing-controlled reactions using pore-scale modeling and micromodel experiments, Environ. Sci. Technol. 42 (2008) 3185–3193.
[13] M.Y. Corapcioglu, P. Fedirchuk, Glass bead micromodel study of solute transport, J. Contam. Hydrol. 36 (1999) 209–230.
[14] C.V. Chrysikopoulos, E.T. Vogler, Acoustically enhanced ganglia dissolution and mobilization in a monolayer of glass beads, Transp. Porous Media 64 (2006) 103–121.
[15] E.H. Jones, C.C. Smith, Non-equilibrium partitioning tracer transport in porous media, 2-D physical modeling and imaging using a partitioning fluorescent dye, Water Res. 39 (2005) 5099–5111.
[16] M. McKellar, N.C. Wardlaw, A method of making two-dimensional glass micromodels of pore systems, J. Can. Petrol. 21 (1982) 39–41.
[17] O. Vizika, A.C. Payatakes, Parametric experimental study of forced imbibition in porous media, Phys. Chem. Hydrodyn. 11 (1989) 187–204.
[18] D.G. Avraam, G.B. Kolonis, T.C. Roumeliotis, G.N. Constantinides, A.C. Payatakes, Steady-state two-phase flow through planar and nonplanar model porous media, Transp. Porous Media 16 (1994) 75–101.
[19] D.G. Avraam, A.C. Payatakes, Flow regimes and relative permeabilities during steady-state two-phase flow in porous media, J. Fluid Mech. 293 (1995) 207–236.
[20] J. Bear, Dynamics of Fluids in Porous Media, Dover, 1972.
[21] R.L. Street, G.Z. Watters, J.K. Vennard, Elementary Fluid Mechanics, 7th ed., Wiley, 1996.
[22] S. Bouhairie, A study of the entrapment process in a recirculation flow by video-imaging method. M.S. Thesis, McGill University, Montreal, Canada, 1998.
[23] C.R. Wilke, P. Chang, Correlation of diffusion coefficients in dilute solutions, AIChE J. 1 (1955) 264–270.
[24] R.B. Bird, W.E. Stewart, E.N. Lightfoot, Transport Phenomena, 2nd ed., Wiley, 2002.
[25] C.V. Chrysikopoulos, P.V. Roberts, P.K. Kitanidis, One-dimensional solute transport in porous media with partial well-to-well recirculation: application to field experiments, Water Resour. Res. 26 (1990) 1189–1195.
[26] Y. Sim, C.V. Chrysikopoulos, Analytical solutions for solute transport in saturated porous media with semi-infinite or finite thickness, Adv. Water Resour. 22 (1999) 507–519.
[27] M. Massabó, R. Cianci, O. Paladino, An analytical solution of the advection dispersion equation in a bounded domain and its application to laboratory experiments, J. Appl. Math. 493014 (2011), doi:10.1155/2011/493014.

[28] P.C. Carman, Fluid flow through granular beds, Trans. Inst. Chem. Eng. 15 (1937) 150–156.

[29] A.A. Garrouch, L. Ali, F. Qasem, Using diffusion and electrical measurements to assess tortuosity of porous media, Ind. Eng. Chem. Res. 40 (2001) 4363–4369.

[30] D.A.G. Bruggeman, Berechnung verschiedener physikalischer Konstanten von heterogenen Substanzen, Ann. Phys. (Leipzig) 24 (1935) 636–679.

[31] L. Pisani, Simple expression for the tortuosity of porous media, Transp. Porous Media 88 (2011) 193–203.

[32] Colour Index, vol. 2, 3rd ed., Society of Dyers and Colourists, Bradford, 1971.

[33] EFSA Panel on Food Additives and Nutrient Sources added to Food (ANS), Scientific opinion on the re-evaluation of Azorubine/Carmoisine (E122) as a food additive on request the European Commission, EFSA J. 7 (11) (2009) 1332, doi:10.2903/j.efsa.2009.1332.

[34] C.V. Chrysikopoulos, Artificial tracers for geothermal reservoir studies, Environ. Geol. 22 (1993) 60–70.

[35] D.R.F. Harleman, R.R. Rumer, Longitudinal and lateral dispersion in an isotropic porous medium, J. Fluid Mech. 16 (1963) 385–394.

[36] N.-W. Han, J. Bhakta, R.G. Carbonell, Longitudinal and lateral dispersion in packed beds: effect of column length and particle size distribution, AIChE J. 31 (1985) 277–288.

[37] R. Anders, C.V. Chrysikopoulos, Virus fate and transport during artificial recharge with recycled water, Water Resour. Res. 41 (2005) W10415, doi:10.1029/2004WR003419.

[38] J.M.P.Q. Delgado, A critical review of dispersion in packed beds, Heat Mass Transfer 42 (2006) 279–310.

[39] I.A. Vasiliadou, C.V. Chrysikopoulos, Cotransport of *Pseudomonas putida* and kaolinite particles through water saturated columns packed with glass beads, Water Resour. Res. 47 (2011) W02543, doi:10.1029/2010WR009560.

[40] C.A. Aggelopoulos, C.D. Tsakiroglou, Quantifying soil heterogeneity from solute dispersion experiments, Geoderma 146 (2008) 412–424.

[41] A.A. Keller, S. Sirivithayapakorn, C.V. Chrysikopoulos, Early breakthrough of colloids and bacteriophage MS2 in a water-saturated sand column, Water Resour. Res. 40 (2004) W08304, doi:1029/2003WR002676.

[42] J.M.P.Q. Delgado, J.R.F. Guedes de Carvalho, Measurement of the coefficient of transverse dispersion in flow through packed beds for a wide range of values of the Schmidt number, Transp. Porous Media 44 (2000) 165–180.

[43] O.A. Cirpka, A. Olsson, Q. Ju, M.A. Rahman, P. Grathwohl, Determination of transverse dispersion coefficients from reactive plume lengths, Ground Water 44 (2006) 212–221.

[44] R.C. Acharya, A.J. Valocchi, C.J. Werth, T.W. Willingham, Pore-scale simulation and reaction along a transverse mixing zone in two-dimensional porous media, Water Resour. Res. 43 (2007) W10435, doi:10.1029/2007WR005969.

[45] A. Olsson, P. Grathwohl, Transverse dispersion of non-reactive tracers in porous media: a new nonlinear relationship to predict dispersion coefficients, J. Contam. Hydrol. 92 (2007) 149–161.

[46] S. Whitaker, Flow in porous media II: the governing equations of immiscible, two-phase flow, Transp. Porous Media 1 (1986) 105–125.

[47] C.V. Chrysikopoulos, P.K. Kitanidis, P.V. Roberts, Generalized Taylor–Aris moment analysis of the transport of sorbing solutes through porous media with spatially-periodic retardation factor, Transp. Porous Media 7 (1992) 163–185.

[48] C.V. Chrysikopoulos, P.K. Kitanidis, P.V. Roberts, Macrodispersion of sorbing solutes in heterogeneous porous formations with spatially periodic retardation factor and velocity field, Water Resour. Res. 28 (1992) 1517–1529.

[49] R.S. Maier, D.M. Kroll, R.S. Bernard, S.E. Howington, J.F. Peters, H.T. Davis, Pore-scale simulation of dispersion, Phys. Fluids 12 (2000) 2065–2079.

[50] M.A. Theodoropoulou, Dispersion of dissolved contaminants in groundwater: from visualization experiments to macroscopic simulation, Water Air Soil Pollut. 181 (2007) 235–245.